Efficient light-emitting diodes from mixed-dimensional perovskites on a fluoride interface

Baodan Zhao[1,2#], Yaxiao Lian[2#], Linsong Cui[1]*, Giorgio Divitini[3], Gunnar Kusch[3], Edoardo Ruggeri[1], Florian Auras[1], Weiwei Li[3], Dexin Yang[2,4], Bonan Zhu[3], Rachel A. Oliver[3], Judith L. MacManus-Driscoll[3], Samuel D. Stranks[1,5], Dawei Di[1,2]*, Richard H. Friend[1]*

1. Cavendish Laboratory, University of Cambridge, JJ Thomson Avenue, Cambridge, CB3 0HE, United Kingdom
2. State Key Laboratory of Modern Optical Instrumentation, College of Optical Science and Engineering; International Research Center for Advanced Photonics, Zhejiang University, Hangzhou, 310027, China
3. Department of Materials Science & Metallurgy, University of Cambridge, 27 Charles Babbage Road, Cambridge, CB3 0FS, United Kingdom
4. College of Materials & Environmental Engineering, Hangzhou Dianzi University, Hangzhou, 310018, China
5. Department of Chemical Engineering & Biotechnology, University of Cambridge, Philippa Fawcett Drive, Cambridge, CB3 0AS, United Kingdom

[#] These authors contributed equally.

Light-emitting diodes (LEDs) based on halide perovskites have recently reached external quantum efficiencies of over 20%. However, the performance of visible perovskite LEDs has been hindered by non-radiative recombination losses and limited options for charge-transport materials that are compatible with the perovskite deposition. Here, we report efficient green electroluminescence from mixed-dimensional perovskites deposited on a thin (~1 nm) lithium fluoride layer on an organic semiconductor hole-transport layer. This highly polar dielectric interface acts as an effective template for forming high-quality bromide perovskites on otherwise incompatible hydrophobic charge-transport layers. Control of crystallinity and dimensionality of the perovskite layer is achieved by using tetraphenylphosphonium chloride as an additive, leading to external photoluminescence quantum efficiencies of around 65%. We achieve LED external quantum efficiencies of up to 19.1% at high brightness (>1500 cd m^{-2}). Our findings provide a strategy for the deposition and device integration of high-quality perovskite semiconductors with improved optoelectronic performance.

Metal halide perovskites are an emerging class of solution processable materials that have exhibited remarkable optoelectronic properties, such as high carrier mobility[1], long diffusion length[2,3], bandgap tunability[4,5], high luminescence efficiency[6] and narrow emission bandwidth[7]. These properties, along with the ease of preparation of halide perovskite materials, have led to great advances in applications such as solar cells[8–11], photodetectors[12,13] and light-emitting diodes (LEDs)[14–17]. The development of perovskite LEDs (PeLEDs) has, in particular, been rapid: in 2014 we reported electroluminescence (EL) from halide perovskites[14] and by 2018 we and others had achieved external quantum efficiencies of >20%[18–21].

We have shown that the internal quantum efficiencies (IQEs) of some of these LEDs approach unity under conventional optical models[18]. This was possible due to improved radiative processes and suppressed non-radiative recombination processes. One of the most successful approaches to enhance the radiative processes in PeLEDs is via charge-carrier confinement within low-dimensional structures, including perovskite nanocrystals[22,23] and mixed-dimensional perovskite nanostructures[16–18]. Suppression of non-radiative recombination processes in PeLEDs has been an equally important strategy, through, for example, the use of polymers[18] and small organic molecules[24,25] as passivating agents for light-emitting perovskites.

Despite the high electroluminescence efficiencies achieved using the reported passivation approaches and device architectures, the possibilities of fabricating high-efficiency perovskite LEDs with structures similar to solution-processed OLEDs[26] remain limited. Due to the strong hydrophobicity of hole-transporting conjugated polymers such as poly(9,9-dioctylfluorene-*alt*-*N*-(4-*sec*-butylphenyl)diphenylamine) (TFB), poly(*N*-(4-butylphenyl)diphenylamine) (poly-TPD) and poly(9,9-dioctylfluorene) (PFO), it is difficult to achieve the subsequent solution deposition of halide perovskite layers. Various approaches have been developed to mediate the formation of perovskite films on conjugated polymers. For example, the surfaces of TFB and poly-TPD hole-transporting layers can be treated using oxygen plasma to convert the surface condition from hydrophobic to hydrophilic before the perovskite deposition[27]. However, this process may cause damage to the surface of the conductive polymer[28], resulting in deteriorated electronic properties. As an alternative solution, it has been shown that a thin interlayer of poly(9-vinylcarbazole) (PVK) can be deposited on the conjugated polymer to allow the deposition of perovskite[29]. PVK is also soluble in *N*,*N*-dimethylformamide (DMF) and dimethyl sulfoxide (DMSO), typical solvents for perovskite precursors, and hence this can lead to intermixing of the perovskite and PVK layers, limiting the reliability of device fabrication.

In this Article, a quasi-2D/3D mixed-dimensional perovskite system to overcome the low external photoluminescence quantum efficiency (PLQE) of 3D perovskite and maintain a decent charge injection ability comparing to perovskite quantum dots. We show that an ultrathin (~1 nm) layer of lithium fluoride (LiF), an ionic compound with strong polarity, can enable perovskite growth on top of polymeric hole-transporting layers. The LiF layer improves the crystal quality and carrier lifetime of perovskite films, leading to enhanced device performance for green PeLEDs based on mixed-dimensional perovskites. The LiF layer acts as an effective template for the growth of high-quality mixed-dimensional perovskite semiconductors. We show that green PeLEDs using mixed-dimensional perovskites on LiF-coated hole-transport layers exhibit EQEs of up to 19.1% with a brightness of >1500 cd m^{-2}. Our mixed-dimensional perovskites with a predominant 3D character show similar or superior performance compared to more 2D-like perovskite heterostructures.

Preparation of emissive perovskite films with TPPCl additive

To achieve a basic quasi-2D/3D composition, we blended phenylethylammonium bromide (PEABr) with the standard precursors of $CsPbBr_3$ 3D perovskite. The molar ratio of the perovskite precursors: lead bromide ($PbBr_2$); caesium bromide (CsBr); and PEABr, in the precursor solution in DMSO was 5:5:2 (Methods). After standard spin-coating and annealing

procedures, uniform perovskite films and bright photoluminescence (PL) were achieved. The PLQE was improved from ~1% for standard $CsPbBr_3$ to 12% for the mixed-dimensional perovskite. We explored the use of additives to control film growth and structure and found that tetraphenylphosphonium chloride (TPPCl) (Fig. 1a) has beneficial effects. The absorption and PL spectra of the perovskite films with and without the TPPCl additive deposited on transparent, electronically inert fused silica substrates are shown in Fig. 1b and Extended Data Figure 1. We observed a reduction of higher-energy excitonic features related to 2D perovskite phases in the absorption spectrum of the perovskite films with TPPCl additive (Fig. 1b) compared to that of the films without TPPCl (Extended Data Figure 1). The additive altered the ratio of 2D and 3D perovskite phases, favouring a higher 3D content. Importantly, we found that the PLQE of the mixed-dimensional perovskite films with the TPPCl additive (61%) was around 5 times of that of the film without TPPCl (12%). The PL kinetics of perovskite film with the TPPCl additive also exhibited a longer lifetime, suggesting that the PLQE improvement was primarily due to suppressed non-radiative decay processes (Fig. 1c). This observation deviates from the model that an energy funnelling/cascade structure involving many 2D phases leads to higher PLQEs)[16,17]. In contrast, we found that TPPCl additive had little effect on the PLQE of standard 3D $CsPbBr_3$ perovskite (Supplementary Table 1).

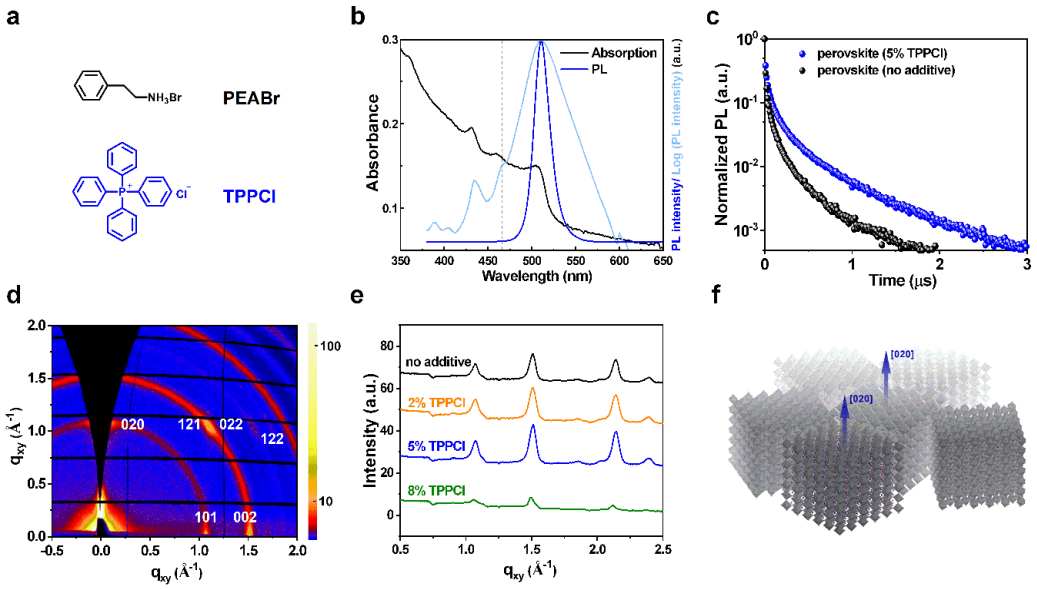

Figure 1 | Effects of the TPPCl additive. a, Chemical structure of the TPPCl additive. **b**, Absorbance and PL spectra of the perovskite film with the TPPCl additive deposited on a fused silica substrate. The dashed lines mark the absorption peaks of the $n = 2$, $n = 3$ and $n \approx \infty$ (3D) phases. The light blue curve is a logarithmic-scale plot of the PL spectrum in linear scale. **c**, PL kinetics of the mixed-dimensional perovskite samples with no additive and with 5% TPPCl inclusion deposited on fused silica substrates. **d**, GIWAXS pattern of the mixed-dimensional perovskite (5% TPPCl) film deposited on a Si substrate. **e**, Radially integrated line profiles over the whole image for perovskite films with different content of TPPCl. **f**, Schematic representation of the orientations of the quasi-3D perovskite domains on the substrate. The *b*-axis is aligned parallel to the substrate normal (i.e., the {020} planes are parallel to the substrate surface), while the individual domains are rotated about the substrate normal.

X-ray photoemission spectroscopy (XPS) and ultraviolet photoemission spectroscopy (UPS) measurements were carried out to study the surface electronic properties. We detected the presence of C, O, Pb, Cs, and Br in the TPPCl-modified mixed-dimensional perovskite samples

through XPS measurements (Extended Data Figure 2). We did not observe any TPPCl or its constituent components on the sample surface. Also, as shown in Supplementary Table 2 and Extended Data Figure 3, the TPPCl additive has a significant impact on the energetics of the perovskite film surfaces. The valance band maximum (VBM) position is elevated from -5.8 eV to -5.2 eV (relative to the vacuum level) as we increase the TPPCl content to 5%, but is lowered again to -5.5 eV for a TPPCl inclusion of 8%. The work function is decreased from -5.0 eV to -4.2 eV (i.e., moved up towards the vacuum level) as the TPPCl inclusion is increased to 8%. We expect the control of band edge positions to allow optimum charge injection at the interfaces. The change in the work function and VBM could be attributed to the reduced quasi-2D components near the surface and/or the altered surface dipoles.

Grazing-incidence wide-angle X-ray scattering (GIWAXS) measurements (Fig. 1d,e and Extended Data Figure 4) indicate that the perovskite films consisted of $CsPbBr_3$ and are highly textured with the {020} planes oriented parallel to the substrate (Fig. 1f and see Extended Data Figure 5 and Supplementary Figure 1 for details). No reflections were observed below q = 1 $Å^{-1}$, suggesting that the $PEA_2CsPb_2Br_7$ (n = 2) and $PEA_2Cs_2Pb_3Br_{10}$ (n = 3) perovskite layers, which can be identified in the absorption and emission spectra, existed as non-periodic (along the stacking direction) phases, potentially incorporated within the $CsPbBr_3$ grains (Extended Data Figure 5d). The addition of the TPPCl also has a significant effect on the perovskite crystallinity (Fig. 1e and Extended Data Figure 4). The reflection intensities increase with increasing TPPCl content of up to 5%, which coincides with the best device performance, while the perovskite film with 8% TPPCl produced significantly weaker reflections; the reduced crystallinity of the 8% sample is also reflected in a reduced EQE of the corresponding LEDs. Extended Data Figure 6 presents an analysis on the radial integrations of the four GIWAXS patterns shown in Extended Data Figure 4. While the TPPCl additive improves the overall crystallinity and the optoelectronic properties, we found that it has little influence on the crystallite orientation.

The effects of the LiF interface

A suitable device architecture is of equal importance for high-performance PeLEDs. As discussed previously, the options for charge-transport materials deposited prior to the spin-coating of the perovskite film are limited by the compatibility of the perovskite precursor solution with the interfacial condition of the substrate. Remarkably, through the insertion of an ultrathin (~1 nm) LiF layer, it is possible to form perovskite films with good luminescent properties on previously incompatible hydrophobic charge-transport materials such as TFB (Extended Data Figure 7). Scanning electron microscopy (SEM) images of a perovskite film with TPPCl on TFB/LiF and oxygen plasma-treated TFB are shown in Fig. 2a. It can be seen that the perovskite film formed on the TFB/LiF interface shows larger and more defined crystal grains and a reduced pinhole density compared to the perovskite film formed on the oxygen plasma-treated TFB surface.

The improved crystallinity of the perovskite deposited on the TFB/LiF interface is also observed in the X-ray diffraction (XRD) patterns of the respective films (Fig. 2b). As discussed above, the perovskite film is highly textured and thus only the (020) and (040) reflections are

observed at 15.2° and 30.4°, respectively, in this one-dimensional measurement. The addition of up to 5% TPPCl causes a slight reduction in the average domain size (Supplementary Table 3), while the peak intensities remain comparable (Supplementary Figure 2) or even improve (Fig. 1e). Using a LiF-modified substrate[30] leads to significantly larger crystallites, consistent with the SEM images in Fig. 2a. It should be noted, however, that the luminescence performance is not directly related to the crystallite size, but rather depends on the reduction of bulk and surface defects (achieved with the combination of the TPPCl additive and LiF-modified interfaces).

The PLQEs of the perovskite films formed on the LiF interface reached 65%, significantly higher than the samples formed on the oxygen plasma-treated TFB and even higher than that of the samples deposited on fused silica. The high PLQEs are in agreement with the slower PL decay of the samples on the LiF interface (Fig. 2c). The PL decay tail lifetime may be associated with the rate of non-radiative monomolecular recombination[18]. The long PL decay tail lifetimes of up to ~0.8 μs (Supplementary Table 4) are an indication of defect-assisted non-radiative processes being well suppressed.

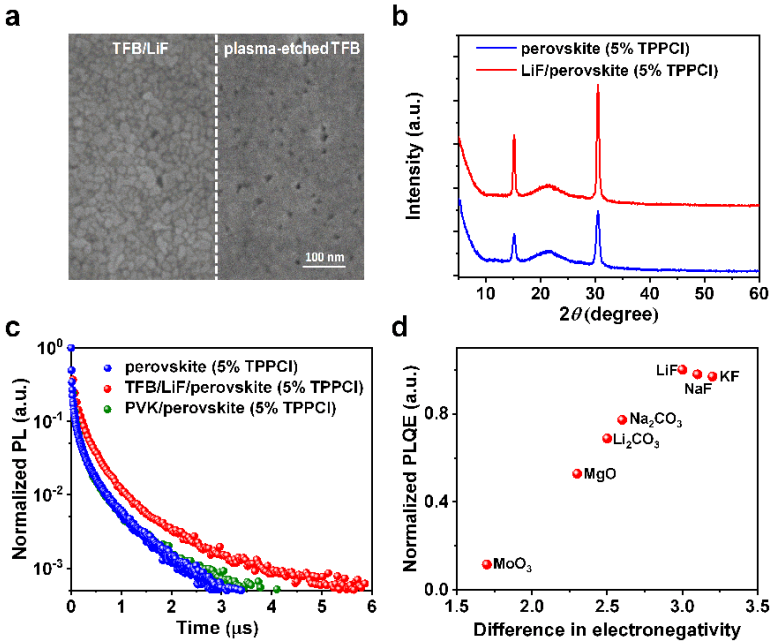

Figure 2 | Effects of the LiF interfacial modifier. a, Scanning electron microscopy (SEM) images of perovskite films deposited on TFB/LiF and plasma-treated TFB. **b**, XRD patterns of perovskite films deposited on LiF-coated (red) an uncoated (blue) fused silica substrates. The broad reflection signal around 20° originates from the fused silica substrate. **c**, PL kinetics of the TPPCl-modified perovskite films on different interfaces: TFB/LiF (red), PVK (green), and uncoated fused silica (blue). The same dataset forming the blue curve is also shown in Fig. 1c. **d,** Normalized PL quantum efficiencies of perovskite films formed on a range of thermally-evaporated interfacial materials with different polarities, characterized by the relative electronegativity of the chemical bonds.

To further understand the possible role of the LiF interface, we prepared perovskite luminescent films deposited on a range of thermally-evaporated interfaces. It is very interesting to note that the luminescent quantum efficiencies of the perovskite films have a strong correlation with the difference in electronegativity of the bonding elements. The results are shown in Fig. 2d. The results imply that strongly polar interfaces may provide an effective

template for forming perovskite films with good luminescent qualities. While such correlation is observed, we cannot completely rule out the possibility of chemical reaction between the perovskite and some of these interlayer materials, which may lead to the variation in PLQE. LiF was normally paired with Al to work as a cathode material for OLEDs[26] and PeLEDs[15] or was deposited on top of the already-formed perovskite layer to achieve surface passivation[31]. In the contrary, in this work LiF is deposited on TFB, a hole-transporting conjugated polymer, to enable subsequent perovskite deposition on the hydrophobic surface, and to allow highly luminescent perovskite films to be formed in new PeLED structures.

Fabrication and characterization of perovskite LEDs

We fabricated perovskite LEDs with a structure of ITO/TFB/LiF/perovskite/2,2',2"-(1,3,5-benzinetriyl)-tris(1-phenyl-1-*H*-benzimidazole) (TPBi)/LiF/Al, as shown in Fig. 3a. A cross-sectional electron microscopy image of a representative device is shown in Fig. 3b. The hole-transport/electron-blocking layer (HTL/EBL) was formed by a ~10 nm spin-coated layer of TFB[26]. The best-performing devices contained an ultrathin (~1 nm) LiF layer that was thermally evaporated onto the HTL (see discussion above). The emissive layer was formed by a ~50 nm thick mixed-dimensional 2D/3D perovskite film with 5% TPPCl. A 50 nm thermally evaporated layer of TPBi serves as the electron-transport/hole blocking layer (ETL/HBL)[32,33], followed by LiF/Al electrodes. A discontinuity in contrast appears between TPBi and perovskite (Fig. 3b), suggesting the presence of a layer with potentially different characteristics. As frequently observed with spin-coated crystalline films, the grains become larger and more well-oriented towards the top surface, which could account for the contrast variation. This is in line with the GIWAXS analysis (Fig. 1d-f) and SEM data (Fig. 2a). Additionally, local heating during the subsequent deposition of the TPBi layer could have induced a partial recrystallization of the perovskite surface, which might contribute to the passivation of electronic defects at the interface.

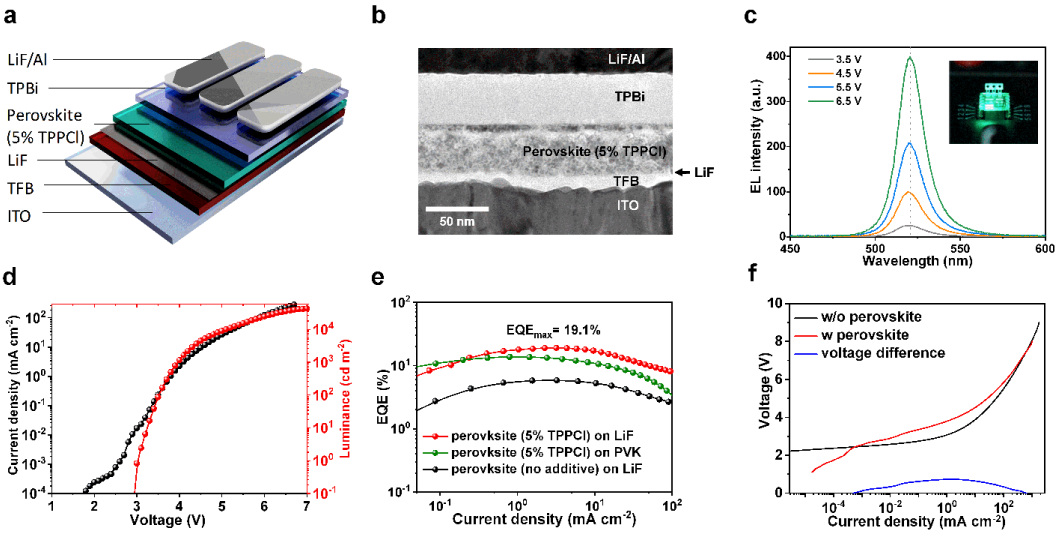

Figure 3 | Characterization of PeLED performance. a, Schematic of the optimised PeLED device structure. **b**, Transmission electron microscopy (TEM) image of the optimised PeLED structure. **c**, The EL spectra across a range of operating voltages from 3.5 V to 6.5 V. **d**, Current-voltage and luminance-voltage characteristics. **e**, EQE curve of the best PeLED. **f,** Comparison of voltage-current characteristics between devices with structures of ITO/TFB/LiF/perovskite (5% TPPCl)/TPBi/LiF/Al and ITO/TFB/LiF/TPBi/LiF/Al.

The electroluminescence (EL) from the PeLED, as shown in Fig. 3c, peaks at ~520 nm with a FWHM of ~18 nm (Fig. 3c), giving high-colour-purity green emission. We did not observe any change in the EL spectra across a range of operating voltages (3.5 V-6.5 V). At voltages of >3 V, the luminance-voltage curve generally follows the current-voltage characteristics on the scales of interests (Fig. 3d), suggesting balanced electron and hole injection. Furthermore, the peak EQE of our best device reaches 19.1% at 3.1 mA cm^{-2} (Fig. 3e), representing a record for green PeLEDs based on mixed-dimensional perovskite system. A luminance of >1500 cd m^{-2} is achieved at the maximum EQE point. The angular emission data of the LEDs closely resembles the Lambertian profile (Extended Data Figure 8a), confirming the peak EQEs are not overestimated. The black curve in Fig. 3e shows the EQE-current characteristics of a PeLED based on perovskite without the TPPCl additive, which shows a much lower peak EQE of 5.8%.

As metal halide perovskites can be simply processed from solution, early PeLED designs were heavily inspired by solution-processed OLED structures[14,15] The poor stability of PeLEDs was partly attributed to the high driving voltages which may give rise to detrimental ion migration[34]. Here, we briefly discuss a key difference between the operation of PeLEDs and OLEDs. For OLEDs, the mobilities of the emissive layer are lower or comparable to those of the charge-transport layers. This leads to a substantial voltage drop across the emissive layer of an organic diode. On the contrary, in PeLEDs the charge carrier mobility of the emissive perovskite layer (typically on the order of 1-10 cm^2 V^{-1} s^{-1})[1] is much higher than that of the organic charge-transport layers (typical values: 10^{-6}-10^{-2} cm^2 V^{-1} s^{-1})[35]. As shown in Fig. 3f and Extended Data Figure 8b-d, we compared the voltage-current characteristics of our optimized device with a similarly-prepared device without the perovskite active layer (ITO/TFB/LiF/TPBi/LiF/Al). This device showed blue EL (from the TFB layer) that arose from electron-hole recombination near the LiF interface. The similar current-voltage characteristic illustrates the low voltage drop expected across the perovskite layer. In particular, we attribute the similar current-voltage behaviour at high current densities to unipolar space charge limited currents in the organic layers. This therefore provides predictable control of the current-voltage characteristics. Lowering the operating voltages is an important issue for PeLEDs[36], and we found that the LiF interlayer is beneficial for lowering the operating voltages in the current device structure (Extended Data Figure 8d).

Cathodoluminescence hyperspectral imaging analysis

Cathodoluminescence (CL) hyperspectral imaging was employed to study the emission energy and intensity properties of the prepared perovskite thin films on the nanoscale. Perovskite films show significant sensitivity to electron beam exposure, potentially damaging the thin films by introducing defects[37] or altering the chemical composition due to beam-induced sample heating[37,38]. To reduce the impact of these detrimental effects, we limited the beam current to 15 pA, which was achieved by using the imaging system in pulsed mode.

Fig. 4a-f show the highest luminescence intensity, lowest roughness for the film deposited on LiF and the lowest intensity, highest roughness for the film without the TPPCl additive as

evident in Extended Data Figure 9 and Supplementary Table 5. More detailed nanoscopic variations of luminescence could not be resolved due to the low-dose pulsed electron beam used during the CL measurements to prevent degradation of the perovskite films. The trends from the CL results are also consistent with the PLQE measurement. The influence of non-radiative defect centres was strongly limited for the sample grown on LiF, having a much smaller capture cross-section. This observation was strengthened by CL lifetime measurement (Extended Data Figure 10), where the LiF sample showed the longest lifetime, again indicating a reduced impact of non-radiative recombination channels within the sample. The rapid CL decay likely results from the local high-power excitation, which exceeds the threshold for Auger recombination.

We noted that for samples without the LiF interface (Fig. 4d,e), their CL peak exhibited a 5-8 nm blue shift relative to their PL peak. This blue shift did not occur in samples grown on LiF interface (Fig. 4f). Several processes are known to occur in perovskite films during the measurements; we consider that the spectral shift may be related to band filling under high injection conditions[14], self-filtering of luminescence[18], local electromigration of halide species and beam damage.

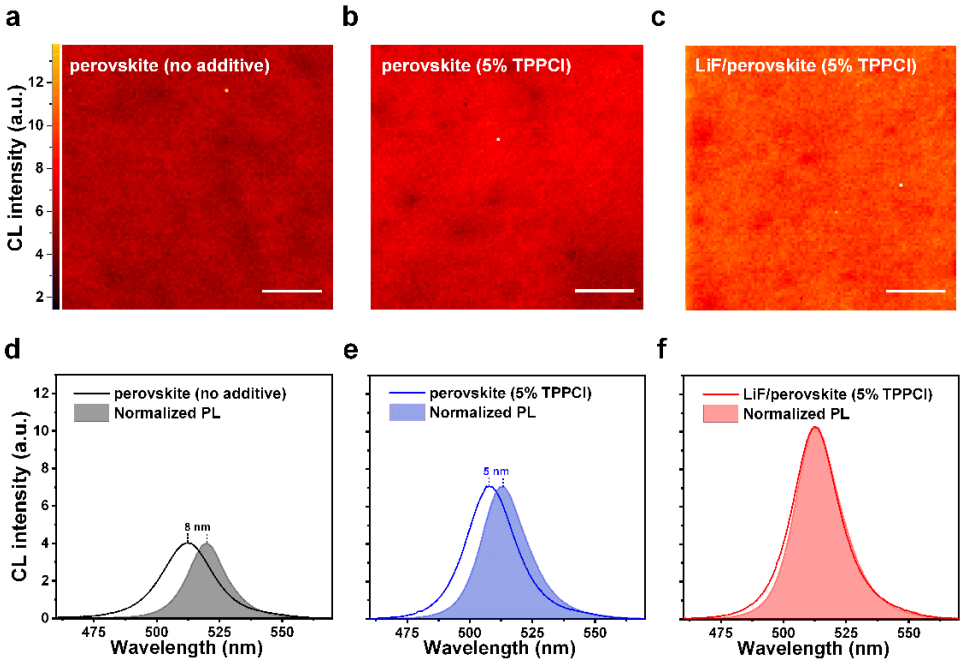

Figure 4 | Cathodoluminescence (CL) mapping of perovskite films. a-c, CL mapping of perovskite films with no additive **(a)**, with 5% TPPCl **(b)**, and with 5% TPPCl on LiF-coated substrate **(c)**, the scale bar is 1 µm. **d-e**, CL spectra (averaged) and the normalized PL spectra (curves enclosing the shaded areas) of perovskite films with no additive (**d**), with 5% TPPCl (**e**), and with 5% TPPCl on LiF-coated substrate (**f**).

Conclusions

We have shown that green LEDs with EQEs of up to 19.1% at high brightness (>1500 cd m^{-2}) can be created by using mixed-dimensional perovskites formed on LiF-coated hole-transport polymers. High-resolution spatial and time-resolved CL measurements confirm that improved luminescence efficiency and uniformity of the film are realised using the combination of the LiF interface and the TPPCl additive. The TPPCl additive modulates the composition of the

mixed-dimensional perovskites, improving the luminescent properties of the emissive films. Introducing a strongly polar interface with an ultrathin (~1 nm) dielectric layer of LiF enables the deposition of highly luminescent perovskite films with improved morphology and crystallinity, allowing reduced interfacial non-radiative losses and efficient hole injection from hole-transporting contacts. Our method allows high-quality perovskite films to be formed on a range of hydrophobic charge-transport materials and previously incompatible substrates, providing a strategy for making high-efficiency PeLEDs with structures similar to solution-processed OLEDs[26,39]. The versatility of device architectures enabled by this approach could accelerate the development of PeLEDs and other perovskite-based optoelectronic devices.

Methods

Preparation of the perovskite precursor solution

The perovskite precursor solution (molar ratio 5:5:2) was prepared by dissolving 110 mg lead bromide ($PbBr_2$) (99.999%, Sigma-Aldrich), 64 mg caesium bromide (CsBr) (99.99%, Sigma-Aldrich), and 24 mg 2-phenylethylammonium bromide (PEABr) (Dyesol) in 1 mL dimethylsulfoxide (DMSO) (Sigma-Aldrich) and stirring overnight at room temperature.

Fabrication of PeLEDs

Pre-patterned indium tin oxide (ITO) substrates (15 ohms/square, Colorado Concept Coatings) were cleaned using ultra-sonication in acetone and isopropanol for 15 min, respectively, and then dried with a nitrogen blow gun, after which the substrates were treated under oxygen plasma etching (forward power: 300 W, reflected power: 0 W, 10 min). The ITO substrates were then transferred to a nitrogen-filled glovebox. TFB was spun from chlorobenzene solution (6mg mL^{-1}) at RPM 3000 and was annealed at 120 ˚C for 10 min. 1 nm of LiF was then evaporated at a pressure of 10^{-6} mBar. Subsequently, the perovskite was spin-coated from the precursor solution to form a ~50 nm layer using a coating speed of 5000 RPM and was annealed at 70 ˚C for 5 min. Finally, TPBi (50 nm), LiF (1 nm) and Al (80 nm) were sequentially evaporated through a shadow mask (area of an active pixel: 4.5 mm^2) at a pressure of 10^{-6} mBar. All the devices were encapsulated with UV epoxy (NOA81, Thorlabs)/cover glass to avoid exposure to oxygen and moisture and degradation during measurement.

SEM measurements

SEM measurements were carried out on perovskite films deposited on fused silica substrates using a high-resolution scanning microscope (LEO GEMINI 1530VP FEG-SE).

Grazing-incidence wide-angle X-ray scattering (GIWAXS)

Grazing-incidence wide-angle X-ray scattering measurements were collected at beamline I07 of the Diamond Light Source facility in Didcot (United Kingdom). The beam energy was 10 keV (1.23985 Å). The scattered beam was collected by a Pilatus 2M large area detector, at a sample-detector distance of 0.4 m and calibrated with a silver behenate (AgBe) sample. The incidence angle was kept at 0.1° to achieve surface-preferential probing with a frame exposure

of 1 s. The sample chamber was continuously purged with a 1 l min^{-1} He flow. Data was processed with the DAWN software package.

Characterization of LED performance

Current density-voltage (J-V) characteristics were measured using a Keithley 2400 source-meter unit. The photon flux was measured simultaneously using a calibrated silicon photodiode centred over the light-emitting pixel. The luminance (in cd m^{-2}) of the devices were calculated based on the emission function of the PeLED and on the known spectral response of the silicon photodiode, and the external quantum efficiencies (EQE) of the devices were calculated assuming a Lambertian emission profile[40,41]. EL spectra of the devices were measured using a Labsphere CDS-610 spectrometer. The accuracy of the LED measurement set-up has been previously cross-checked against a third-party industrial laboratory[26].

XRD measurements

XRD measurements were carried out on perovskite films on fused silica substrates using a Bruker X-ray D8 Advance diffractometer with Cu $K\alpha_{1,2}$ radiation (λ = 1.541 Å). Spectra were collected with an angular range of $5° < 2\theta < 60°$.

PLQE measurements

The PLQE of thin-film samples were measured using an integrating sphere method, described elsewhere[42]. A continuous-wave 405-nm diode laser with the excitation power ranging from 0.5 mW to 60 mW and a focused beam spot of ~0.3 mm^2 was used to excite the samples optically. Emission was measured using an Andor iDus DU420A Si detector.

Time-correlated single photon counting (TCSPC) measurements

The perovskite films spin-coated on pre-cleaned fused silica were photo-excited using a 407-nm pulsed laser with pulse width <200 ps, at a repetition rate of 50 kHz-25 MHz. Photons emitted from the sample were detected by a Si-based single-photon avalanche photodiode. The instrument response function has a lifetime of ~0.2 ns. A 420-nm long-pass filter was used to screen-out any scattered laser signal in the optical path.

UPS measurements

UPS was used to determine the work function and valence band maximum of perovskite films. The UPS spectra were acquired in an Omicron ultrahigh-vacuum chamber with excitation provided by the He I emission line (21.2 eV) of a helium discharge lamp. The work function is calculated by Φ = 21.2 – Onset, as shown in Extended Data Figure 3a-d. The VBM is determined by linear extrapolation of the leading edge of the VB to zero baseline intensity, as shown in Extended Data Figure 3e-h. XPS was measured by a monochromatic Al $K\alpha_1$ X-ray source (hv= 1486.6 eV) using a SPECS PHOIBOS 150 electron energy analyzer with a total energy resolution of 500 meV.

Cathodoluminescence (CL) mapping

CL hyperspectral mapping was performed in an Attolight Allalin 4027 Chronos dedicated CL-SEM. CL spectra and images were recorded with an iHR320 spectrometer with a focal length of 320 mm with a 150 l/mm grating blazed at 500 nm a 700 μm entrance slit and an Andor

1024 px charged coupled device. All measurements were performed at room temperature in pulsed mode with an acceleration voltage of 5 kV and a current of 15 pA.

Transient CL mapping

Time resolved CL measurements were performed by pulsing the electron gun with the third harmonic of a ND:YAG laser (355 nm) with a frequency of 80.6 MHz and a pulse width of 7 ps. The streak images were recorded with a Horiba Streak camera at an acceleration voltage of 5 kV and a beam current of 15 pA.

Data Availability. The research data supporting this paper are available in the University of Cambridge Repository (www.repository.cam.ac.uk). Related research results are available from the corresponding authors upon reasonable request.

References

1. Wehrenfennig, C., Eperon, G.E., Johnston, M.B., Snaith, H.J. & Herz, L.M. High charge carrier mobilities and lifetimes in organolead trihalide perovskites. *Adv. Mater.* **26**, 1584–1589 (2014).
2. Stranks, S.D. *et al.* Electron-hole diffusion lengths exceeding 1 micrometer in an organometal trihalide perovskite absorber. *Science* **342**, 341–344 (2013).
3. Xing, G. *et al.* Long-range balanced electron and hole-transport lengths in organic-inorganic $CH_3NH_3PbI_3$. *Science* **342**, 344–347 (2013).
4. Hattori, T., Taira, T., Era, M., Tsutsui, T. & Saito, S. Highly efficient electroluminescence from a heterostructure device combined with emissive layered-perovskite and an electron-transporting organic compound. *Chem. Phys. Lett.* **254**, 103–108 (1996).
5. Mitzi, D.B., Chondroudis, K. & Kagan, C.R. Organic-inorganic electronics. *IBM J. Res. Dev.* **45**, 29–45 (2001).
6. Deschler, F. *et al.* High photoluminescence efficiency and optically pumped lasing in solution-processed mixed halide perovskite semiconductors. *J. Phys. Chem. Lett.* **5**, 1421–1426 (2014).
7. Sutherland, B.R. & Sargent, E.H. Perovskite photonic sources. *Nat. Photonics* **10**, 295–302 (2016).
8. Kojima, A., Teshima, K., Shirai, Y. & Miyasaka, T. Organometal halide perovskites as visible-light sensitizers for photovoltaic cells. *J. Am. Chem. Soc.* **131**, 6050–6051 (2009).
9. Lee, M.M., Teuscher, J., Miyasaka, T., Murakami, T.N. & Snaith, H.J. Efficient hybrid solar cells based on meso-superstructured organometal halide perovskites. *Science* **338**, 643–647 (2012).
10. Kim, H.-S. *et al.* Lead iodide perovskite sensitized all-solid-state submicron thin film mesoscopic solar cell with efficiency exceeding 9%. *Sci. Rep.* **2**, 591 (2012).
11. Green, M.A., Ho-Baillie, A. & Snaith, H.J. The emergence of perovskite solar cells. *Nat. Photonics* **8**, 506–514 (2014).
12. Dou, L. *et al.* Solution-processed hybrid perovskite photodetectors with high detectivity. *Nat. Commun.* **5**, 5404 (2014).
13. Fang, Y., Dong, Q., Shao, Y., Yuan, Y. & Huang, J. Highly narrowband perovskite

single-crystal photodetectors enabled by surface-charge recombination. *Nat. Photonics* **9**, 679–686 (2015).
14. Tan, Z.-K. *et al.* Bright light-emitting diodes based on organometal halide perovskite. *Nat. Nanotechnol.* **9**, 687–692 (2014).
15. Cho, H. *et al.* Overcoming the electroluminescence efficiency limitations of perovskite light-emitting diodes. *Science* **350**, 1222–1225 (2015).
16. Yuan, M. *et al.* Perovskite energy funnels for efficient light-emitting diodes. *Nat. Nanotechnol.* **11**, 872–877 (2016).
17. Wang, N. *et al.* Perovskite light-emitting diodes based on solution-processed self-organized multiple quantum wells. *Nat. Photonics* **10**, 699–704 (2016).
18. Zhao, B. *et al.* High-efficiency perovskite–polymer bulk heterostructure light-emitting diodes. *Nat. Photonics* **12**, 783–789 (2018).
19. Chiba, T. *et al.* Anion-exchange red perovskite quantum dots with ammonium iodine salts for highly efficient light-emitting devices. *Nat. Photonics* **12**, 681–687 (2018).
20. Cao, Y. *et al.* Perovskite light-emitting diodes based on spontaneously formed submicrometre-scale structures. *Nature* **562**, 249–253 (2018).
21. Lin, K. *et al.* Perovskite light-emitting diodes with external quantum efficiency exceeding 20 percent. *Nature* **562**, 245–248 (2018).
22. Di, D. *et al.* Size-dependent photon emission from organometal halide perovskite nanocrystals embedded in an organic matrix. *J. Phys. Chem. Lett.* **6**, 446–450 (2015).
23. Li, G. *et al.* Efficient light-emitting diodes based on nanocrystalline perovskite in a dielectric polymer matrix. *Nano Lett.* **15**, 2640–2644 (2015).
24. Ban, M. *et al.* Solution-processed perovskite light emitting diodes with efficiency exceeding 15% through additive-controlled nanostructure tailoring. *Nat. Commun.* **9**, 3892 (2018).
25. Xu, W. *et al.* Rational molecular passivation for high-performance perovskite light-emitting diodes. *Nat. Photonics* **13**, 418–424 (2019).
26. Di, D. *et al.* High-performance light-emitting diodes based on carbene-metal-amides. *Science* **356**, 159–163 (2017).
27. Xiao, Z. *et al.* Efficient perovskite light-emitting diodes featuring nanometre-sized crystallites. *Nat. Photonics* **11**, 108–115 (2017).
28. Gerenser, L. J. XPS studies of in situ plasma-modified polymer surfaces. *J. Adhes. Sci. Technol.* **7**, 1019–1040 (1993).
29. Si, J. *et al.* Efficient and high-color-purity light-emitting diodes based on *in situ* grown films of $CsPbX_3$ (X = Br, I) nanoplates with controlled thicknesses. *ACS Nano* **11**, 11100–11107 (2017).
30. Shi, Y. *et al*. A Strategy for architecture design of crystalline perovskite light‐emitting diodes with high performance. *Adv. Mater.* 30, 1800251 (2018).
31. Stolterfoht, M. et al. Visualization and suppression of interfacial recombination for high-efficiency large-area pin perovskite solar cells. *Nat. Energy* **3**, 847–854 (2018).
32. Yeh, S.-J. *et al.* New dopant and host materials for blue-light-emitting phosphorescent organic electroluminescent devices. *Adv. Mater.* **17**, 285–289 (2005).
33. Aizawa, N. *et al.* Solution-processed multilayer small-molecule light-emitting devices

with high-efficiency white-light emission. *Nat. Commun.* **5**, 5756 (2014).
34. Chen, M., Shan, X., Geske, T., Li, J. & Yu, Z. Manipulating ion migration for highly stable light-emitting diodes with single-crystalline organometal halide perovskite microplatelets. *ACS Nano* **11**, 6312–6318 (2017).
35. Kulkarni, A.P., Tonzola, C.J., Babel, A. & Jenekhe, S.A. Electron transport materials for organic light-emitting diodes. *Chem. Mater.* **16**, 4556–4573 (2004).
36. Sim, K. et al. Performance boosting strategy for perovskite light-emitting diodes. *Appl. Phys. Rev.* **6**, 031402 (2019).
37. Xiao, C. *et al.* Mechanisms of electron-beam-induced damage in perovskite thin films revealed by cathodoluminescence spectroscopy. *J. Phys. Chem. C* **119**, 26904–26911 (2015).
38. Divitini, G. *et al.* In situ observation of heat-induced degradation of perovskite solar cells. *Nature Energy* **1**, 15012 (2016).
39. Yang, L., Kim, V., Lian, Y., Zhao, B. & Di, D. High-efficiency dual-dopant polymer light-emitting diodes with ultrafast inter-fluorophore energy transfer. *Joule* 3, 2381–2389 (2019).
40. Greenham, N.C., Friend, R.H. & Bradley, D.D.C. Angular dependence of the emission from a conjugated polymer light-emitting diode: implications for efficiency calculations. *Adv. Mater.* **6**, 491–494 (1994).
41. Forrest, S. R., Bradley, D.D.C. & Thompson, M.E. Measuring the efficiency of organic light-emitting devices. *Adv. Mater.* **15**, 1043–1048 (2003).
42. de Mello, J.C., Wittmann, H.F. & Friend, R.H. An improved experimental determination of external photoluminescence quantum efficiency. *Adv. Mater.* **9**, 230–232 (1997).
43. Stoumpos, C. C. *et al.* Crystal growth of the perovskite semiconductor $CsPbBr_3$: A new material for high-energy radiation detection. *Cryst. Growth Des.* **13**, 2722–2727 (2013).
44. Shibuya, K., Koshimizu, M., Nishikido, F., Saito, H. & Kishimoto, S. Poly[bis(phenethylammonium) [dibromidoplumbate(II)]-di-μ-bromido]]. *Acta Crystallogr. Sect. E Struct. Reports Online* **65**, m1323–m1324 (2009).

Acknowledgements

This work was supported by the National Key Research and Development Program of China (grant no. 2018YFB2200401), the National Natural Science Foundation of China (NSFC) (61975180, 51702289), the Fundamental Research Funds for the Central Universities (2019QNA5005), and Zhejiang University Education Foundation Global Partnership Fund. G.D. acknowledges funding from EU H2020 grant number 823717 – ESTEEM3. R.A.O. and G.K. acknowledge financial support from the EPSRC (under EP/R025193/1) and from Attolight. Dr Christian Monachon of Attolight is thanked for his ongoing support of the TRCL system. E.R. and S.D.S. acknowledge the ERC under the European Union's Horizon 2020 research and innovation program (HYPERION, grant agreement number 756962). E.R. acknowledges partial funding from an EPSRC Departmental Graduate Studentship. S.D.S. acknowledges the Royal Society and Tata Group (UF150033). This work utilized beamline I07 at the Diamond Light Source (Proposal SI17223). W.L. and J.L.M.-D. acknowledge support from EPSRC grant EP/L011700/1, EP/N004272/1, and the Isaac Newton Trust (Minute

13.38(k)). B. Zhu acknowledges support from China Scholarship Council and Cambridge Commonwealth, European and International Trust. This project has received funding from the European Research Council (ERC) under the European Union's Horizon 2020 research and innovation programme (Grant agreement No. 670405). The authors thank the Engineering and Physical Sciences Research Council (EPSRC) for support.

Author contributions

B.Z. and L.C. planned the project under the guidance of D.D and R.H.F. B.Z. and L.C. developed and characterized the high-efficiency LEDs. Y.L. performed experiments and analyses related to LiF and other polar interfaces. B.Z. and L.C. carried out the PL, PLQE, ns-μs transient PL, XRD and SEM studies. F.A. built the crystalline structure model based on XRD results. Y.L. and D.Y. performed the cross-sectional TEM studies. E.R. carried out the GIWAX measurements and analysis. G.D., G.K. and B.Z. performed the CL mapping and transient CL studies. G.D. analysed the CL results. W.L. analysed the UPS and XPS results. B.Z. and D.D. wrote the manuscript, which was revised by R.H.F. All authors contributed to the work and commented on the paper.

Competing interests

The authors declare no competing interests.

Corresponding authors

Correspondence to: Richard H. Friend (rhf10@cam.ac.uk), Dawei Di (daweidi@zju.edu.cn), or Linsong Cui (lc724@cam.ac.uk).